AFRL-AFOSR-VA-TR-2019-0352

Chiral Nanophotonics

Federico Capasso
HARVARD COLLEGE PRESIDENT & FELLOWS OF

07/11/2019
Final Report

Air Force Research Laboratory
AF Office Of Scientific Research (AFOSR)/ RTB1
Arlington, Virginia 22203
Air Force Materiel Command

DISTRIBUTION A: Distribution approved for public release.

REPORT DOCUMENTATION PAGE

Form Approved
OMB No. 0704-0188

1. REPORT DATE *(DD-MM-YYYY)*	2. REPORT TYPE	3. DATES COVERED *(From - To)*
21-11-2019	Final Performance	01 Apr 2016 to 31 Mar 2019

4. TITLE AND SUBTITLE
Chiral Nanophotonics

5a. CONTRACT NUMBER

5b. GRANT NUMBER
FA9550-16-1-0156

5c. PROGRAM ELEMENT NUMBER
61102F

6. AUTHOR(S)
Federico Capasso

5d. PROJECT NUMBER

5e. TASK NUMBER

5f. WORK UNIT NUMBER

7. PERFORMING ORGANIZATION NAME(S) AND ADDRESS(ES)
HARVARD COLLEGE PRESIDENT & FELLOWS OF
1350 MASS AVE STE 600
CAMBRIDGE, MA 02138-3846 US

8. PERFORMING ORGANIZATION REPORT NUMBER

9. SPONSORING/MONITORING AGENCY NAME(S) AND ADDRESS(ES)
AF Office of Scientific Research
875 N. Randolph St. Room 3112
Arlington, VA 22203

10. SPONSOR/MONITOR'S ACRONYM(S)
AFRL/AFOSR RTB1

11. SPONSOR/MONITOR'S REPORT NUMBER(S)
AFRL-AFOSR-VA-TR-2019-0352

12. DISTRIBUTION/AVAILABILITY STATEMENT
A DISTRIBUTION UNLIMITED: PB Public Release

13. SUPPLEMENTARY NOTES

14. ABSTRACT
The PI and his group opened new directions of research in chiral nanophotonics by investigating theoretically and experimentally the interaction of chiral light (circularly and elliptically polarized) with both individual and ensembles, known as metasurfaces, of chiral anoparticles/nanostructures, engineered using advanced nanofabrication techniques and measured with broadband (visible to near infrared) far field and nearfield optical techniques. This includes: an in-depth study of chiral holograms and their ability to project vastly different images depending on the chirality of light; multispectral chiral imaging with a metalens; ultracompact chiral spectrometer functionalities with metalenses; the demonstration of giant intrinsic chirooptical activity in planar dielectric nanostructures orders of magnitude higher than previously reported; metasurface polarization optics that enables to achieve different functionalities depending on the polarization of incident light; arbitrary spin-to-orbital angular momentum conversion in metasurfaces as a new route to creating structured light.

15. SUBJECT TERMS
chiral nanophotonics, chirality, plasmon polaritons, plasmon, polarization, optical forces, nanostructures, interconnects

16. SECURITY CLASSIFICATION OF:			17. LIMITATION OF ABSTRACT	18. NUMBER OF PAGES	19a. NAME OF RESPONSIBLE PERSON
a. REPORT	b. ABSTRACT	c. THIS PAGE			POMRENKE, GERNOT
Unclassified	Unclassified	Unclassified	UU		19b. TELEPHONE NUMBER *(Include area code)* 703-696-8426

Standard Form 298 (Rev. 8/98)
Prescribed by ANSI Std. Z39.18

Performance Report AFOSR

AFOSR Grant Number: FA9550-16-1-0156
Chiral Nanophotonics

Reporting Period: 04/01/2016 – 03/31/2019

PI: Prof. Federico Capasso
School of Engineering and Applied Sciences Harvard University
205A Pierce Hall 29 Oxford St.
Cambridge MA 02138
Tel. 617-3847611
Fax 617-495-2875
Email: capasso@seas.harvard.edu

1. Objectives

The overarching goal was to investigate theoretically and experimentally the interaction of chiral light (i.e. circularly and elliptically polarized) with both individual and ensembles (i.e. metasurfaces) of chiral nanoparticles/nanostructures, engineered using advanced nanofabrication techniques and measured with broadband (visible to near infrared) far field and nearfield imaging techniques. This includes: (1) an in-depth study of chiral holograms and their ability to project vastly different images depending on the chirality of light; (2) multispectral chiral imaging with a metalens; (3) chiral spectrometer functionalities with metalenses; (4) intrinsic chiro-optical activity in planar dielectric nanostructures; (5) metasurface polarization optics; (6) Spin-to-orbital angular momentum conversion in metasurfaces

2. Summary of accomplishments

The fundamental element for these studies is an anisotropic nanofin acting as a half wave plate. The response of this structure is inherently chiral meaning that for incident circular polarization of one chirality (e.g. right circularly polarized) the transmitted light gets entirely converted into light of the opposite chirality (e.g. left circularly polarized. Most importantly the transmitted field acquires a phase factor $\exp(2i\alpha)$, known as Berry phase, where α is the rotation angle of the fin with respect to an arbitrary reference axis. Thus, differently oriented fins assembled in a subwavelength spaced array (metasurface) can be arranged to create arbitrary phase profiles $\varphi(x,y)$ depending on the distribution of the rotation angle $\alpha(x,y)$. For example, if $\alpha(x,y)=q\theta$ where θ is the azimuthal angular position a vortex beam with a helical phase $\exp(i2q\theta)$ will be created. Similarly, the phase profile of a lens and in general any hologram can be created by choosing the proper arrangements of the fins. In these examples every nanofin was assumed to have the same propagation phase, so that the wavefront is only affected by the Berry phase. If the former is also changed with position an additional design degree of freedom is created that can be used to create a whole new class of phase plates with local control of the nanofins shape birefringence. In this way the polarization of light can be locally controlled in addition to the phase and amplitude making it possible to explore new forms of structured light and new design functionalities. Many of these possibilities where explored in this contract leading to discovery of new optical phenomena and the realization of new optical components.

A. Broadband and chiral dielectric holograms

Shaping the wavefront of light is the basic principle of any optical component and has been accomplished iin phase holograms by locally modulating the phase of incident light. Traditionally, phase modulation has been achieved by spatially modifying the refractive index of a bulk host medium. Using subwavelength resonators/ scatterers metasurfaces enable wavefront modulation in a thin and compact configuration. These are very crucial for realization of miniaturized multifunctional optical components, which are in high demand for applications ranging from mobile devices to space mission apparatus where the combination of high quality and small footprint is demanding. However, in most metasurfaces implementation, the wavelength response is highly dispersive limiting in fact their operation bandwidth. Here, we engineered the dispersive response of dielectric waveguides to realize efficient and broadband holographic devices.

B. Multispectral chiral imaging with a metalens

Most biologically active compounds, ranging from amino acids to essential nutrients such as glucose, possess intrinsic handedness. This in turn gives rise to chiral optical properties that provide a basis for detecting and quantifying enantio-specific concentrations of these molecules. However traditional chiroptical spectroscopy and imaging techniques require cascading of multiple optical components in sophisticated setups to extract information from specimens. We have demonstrated a planar lens with an engineered dispersive response, which simultaneously forms two images with opposite helicity of an object within the same field-of-view. In this way, chiroptical properties can be probed across the visible spectrum using only the lens and a camera without the addition of polarizers or dispersive optical devices. Using this planar lens, we mapped the circular dichroism of the exoskeleton of a chiral beetle, *Chrysina gloriosa,* known to exhibit high reflectivity of left-circularly polarized light with high spatial resolution limited only

by the numerical aperture of the lens. Our results demonstrated the potential of metasurfaces in realizing a compact and multifunctional device with unprecedented imaging capabilities.

C. Ultra-compact visible chiral spectrometer with metalenses

Conventional compact spectrometers have a fixed spectral resolution and cannot resolve the polarization properties of light without additional optical elements, while their larger counterparts are bulky and costly. We demonstrated multiple off-axis meta-lenses in the visible integrated on a single planar substrate. They possess both focusing and strongly dispersive properties and are designed to provide different spectral resolutions as well as working wavelength ranges on the same chip. We realized a compact spectrometer using only these meta-lenses and a CMOS camera and achieved detector-limited spectral resolutions as high as 0.3 nm and a total working wavelength range exceeding 170 nm for a beam propagation length of only a few cm. In addition, this spectrometer has the capability to resolve different helicities of light in a single measurement. This chip-camera setup represents the most compact configuration so far achieved for a spectrometer with similar performance and functionality, and its compatibility with large-scale fabrication processes makes it broadly applicable.

D. Giant intrinsic chiro-optical activity in planar dielectric nanostructures

The strong optical chirality arising from certain synthetic metamaterials have important and widespread applications in polarization optics, stereochemistry and spintronics. However, these intrinsically chiral metamaterials are restricted to a complicated three-dimensional (3D) geometry which leads to significant fabrication challenges, particularly at visible wavelengths. Their planar two-dimensional (2D) counterparts are limited by symmetry considerations to operation at oblique angles (extrinsic chirality) and possess significantly weaker chiro-optical responses close to normal incidence. Here we address the challenge of realizing strong intrinsic chirality from thin, planar dielectric nanostructures. Most notably, we experimentally achieve near-unity circular dichroism with approximately 90% of the light with the chosen helicity being transmitted at 540 nm wavelength. This is the highest value demonstrated to date for any geometry in the visible spectrum. We show that the excitation of higher-order multipoles is responsible for the giant circular dichroism.

E. Metasurface polarization optics: independent phase control of arbitrary orthogonal states of polarization

We have recently presented a method that allows for the imposition of two independent and arbitrary phase profiles on any pair of orthogonal states of polarization—linear, circular, or elliptical—relying only on simple, linearly birefringent wave plate elements arranged into metasurfaces. Using this approach, we demonstrated chiral holograms characterized by fully independent far fields for each circular polarization and in addition elliptical polarization beam splitters, both in the visible. This approach significantly expands the functionality of metasurface polarization optics.

F. Spin-to-orbital angular momentum conversion in dielectric metasurfaces

Helical beams (known also as vortex beams) are a variety of chiral beams characterized by a helical wavefront and a phase singularity point on the propagation axis that results in a doughnut-like intensity profile. Spin-to-orbital angular momentum conversion has attracted considerable interest as a tool to create vortex beams. In this process, the geometrical phase is exploited to create helical beams whose handedness is determined by the circular polarization (left/right) of the incident light, hat is by its spin. We demonstrated high-efficiency Spin-to-Orbital angular momentum-Converters (SOCs) at visible wavelengths based on dielectric metasurfaces. With these SOCs we generated vortex beams with high and fractional topological charge and showed for the first time the simultaneous generation of collinear helical beams with different and arbitrary orbital angular momentum.

G. Arbitrary spin-to-orbital angular momentum conversion of light

Optical elements that convert the spin angular momentum (SAM) of light into vortex beams have found applications in classical and quantum optics. These elements, SAM to orbital angular momentum (OAM)

converters, are based on the geometric phase and only permit the conversion of left- and right-circular polarizations (spin states) into states with opposite OAM. We present a method for converting arbitrary SAM states into total angular momentum states characterized by a superposition of independent OAM. We design a metasurface that converts left- and right-circular polarizations into states with independent values of OAM, and another device that performs this operation for elliptically polarized states. These results illustrate a general material-mediated connection between SAM and OAM of light and may find applications in producing complex structured light and in optical communication.

3. Detailed Accomplishments

A. Broadband and chiral dielectric holograms

We use a dispersion free phase shift mechanism based on Berry's phase concept enabling holograms to preserve their functionality across a wide spectral range (from visible to near infrared). Our devices are fabricated by etching silicon nano-structures on a glass substrate (Fig.1 (a), (b). These silicon nano-structures work as building blocks of holographic devices and their birefringence provides additional control over both linear and circular polarization. We demonstrate a chiral hologram in which the projected images depend on the handedness of the incident beam (Fig. 1 (c). Efficiency as high as 75% is experimentally achieved in the near infrared region. Our approach introduces a facile platform for realization of broadband and versatile thin and flat optical components.

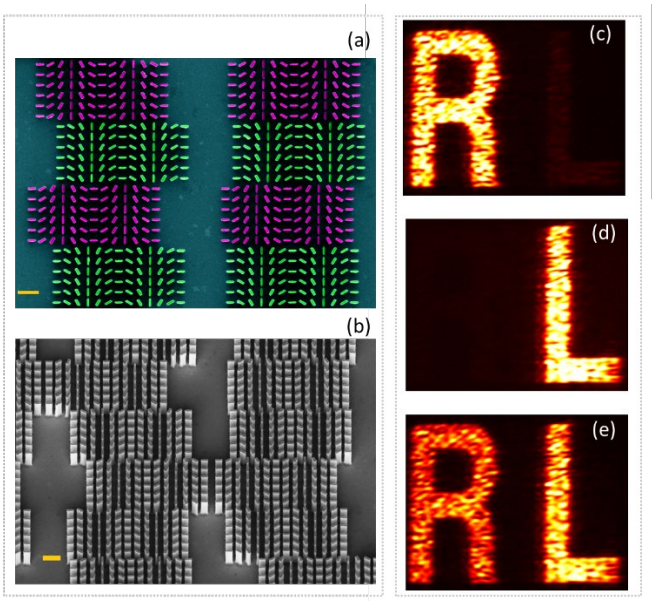

Fig. 1. Chiral hologram. (a) False colored scanning electron micrograph (SEM) of four pixels of the hologram. Each pixel consists of two parts: in purple, those that impart the required phase map for letter "L" and in green, those for the phase map for letter "R". Nanofins have width *W=85 nm*, length *L= 350* nm, height *H=1000 nm*, and center-to-center distance of *500 nm*. The scale bar is 1 μm. (b) Tilted-view: SEM image of the hologram. The scale bar is 1μm. (c)-(e) Images in the +1 diffraction order (false colored) generated by the chiral hologram under different incident polarizations at λ=1350 nm. Chiral hologram illuminated by (c) right-circularly (d) left-circularly and (e) linearly polarized light resulting in the appearance of the letters "*R*", "*L*" and "*RL*", respectively.

B. Multispectral Chiral Imaging with a Planar Lens

Chiroptical spectroscopy and imaging is essential for extracting structural and functional properties of biological species at both molecular and bulk levels. However, such imaging and spectroscopy systems require cascading of multiple optical components to extract valuable chiral and spectral information from a specimen. We demonstrated a planar chiral lens capable of performing chiroptical spectral analysis with nothing more than a CCD camera. Our results demonstrate the potential of a metasurface in realizing a compact, multifunctional device with unprecedented imaging performance. We have designed a meta-lens based on titanium dioxide nanostructures that forms two images of opposite helicities. Figure 1(a-e) shows the design and fabrication based on the Berry Phase given locally by twice the fin rotation angle.

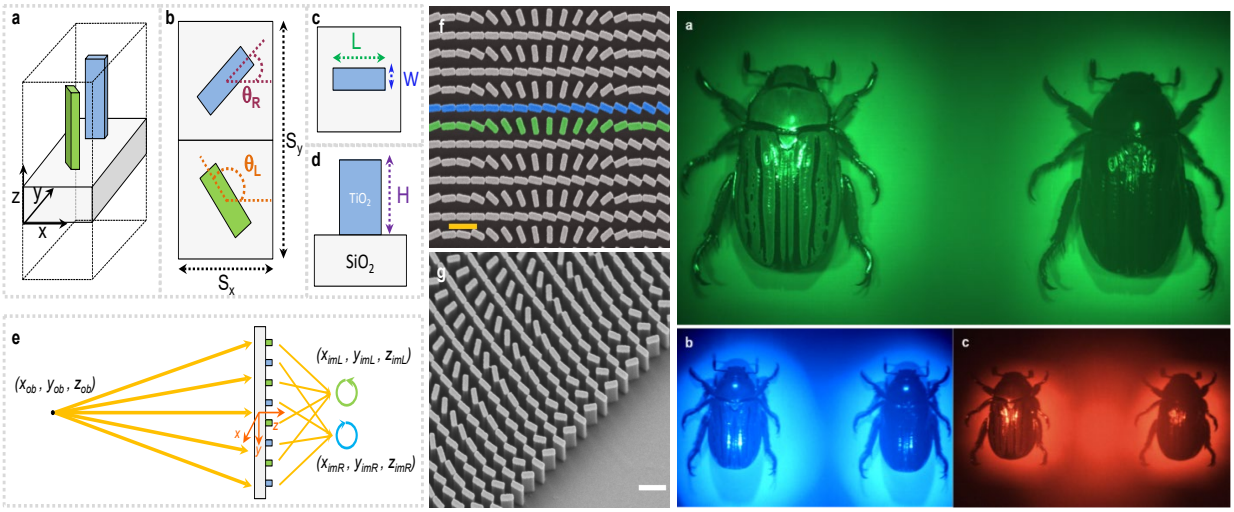

Fig. 2. Multispectral chiral lens (MCHL). *Left Panel:* (a) The building block of the MCHL consists of two nanofins on a glass substrate. (b) Top-view of the building block where S_x=*300 nm* and S_y= *600 nm*. The blue and green nanofins impart the required phase profile required to focus right-circularly polarized (RCP) light and left-circularly polarized (LCP) light, respectively. Phase realization is based on the geometric phase by means of nanofin rotation. (c) Top-view of a nanofin denoting its length *L=250 nm,* and width *W=80 nm*. (d) Side-view of a nanofin showing its height *H= 600 nm*. (e) Schematic diagram illustrating the imaging principle of the MCHL where RCP and LCP light from the same object at coordinates (x_{ob}=*0,* y_{ob}=*0,* z_{ob}=*-18 cm*) are separated and then focused into two spots, (x_{imL}, y_{imL}, z_{imL}) and (x_{imR}, y_{imR}, z_{imR}). Coordinates of these spots are wavelength dependent due to dispersive design of the MCHL.
Right Panel:(a)-(c) The meta-lens forms two images of the beetle in the same field of view on the color camera. The left (right) image is formed by focusing left (right)-circularly polarized light reflected from the beetle. Illumination was provided by green (a), blue (b), and red (c) LEDs paired with 10 nm bandpass filter centered at 532 nm, 488 nm and 620 nm, respectively.

For imaging of a biological specimen across the visible range, we chose *Chrysina gloriosa*, a chiral beetle with naturally strong circular dichroism (CD). Figure 3(a) shows that the meta-lens simultaneously forms two images of the beetle on the camera chip. These images have opposite helicity and their contrast reveals a very strong CD of the beetle exoskeleton. The latter experiment was done under green LED illumination, and repeated for blue and red LEDs as shown in Fig. 3(b) and Fig. 3(c), respectively.

C. Ultra-compact visible chiral spectrometer with meta-lenses

We realized a spectrometer based on efficient off-axis metasurface lenses using titanium oxide nanostructures (Fig. 3 (a)). By stitching four off-axis focusing lenses with different focusing angles on a substrate, we achieved high dispersion and spectral resolution within a short propagation distance.

Since these nanostructures impart the desired phase profile using the geometric (Berry) phase, such a device is also chiral – it can distinguish between different helicities of incident circularly polarized light and resolve the spectrum in a single measurement. Since these metalenses act as both focusing and dispersive element, the overall footprint of the spectrometer including the CMOS sensor is significantly reduced and represents the simplest possible configuration for a spectrometer.

The metasurface design is based on form-birefringent half-wave nanofin structures comprising of TiO_2 rotated to provide the required lens phase profile, as previously discussed. We fabricated four metasurface lenses on the same substrate, as shown in Fig. 4(b). The lenses are designed in this way to provide spatially separated focal spots on the same field of view of a CMOS camera, while possessing different spectral resolution, effective working range and different helicities of circular polarization. Two focal spots belonging to one helicity are characterized as shown in Fig. 4(c), demonstrating diffraction-limited focusing.

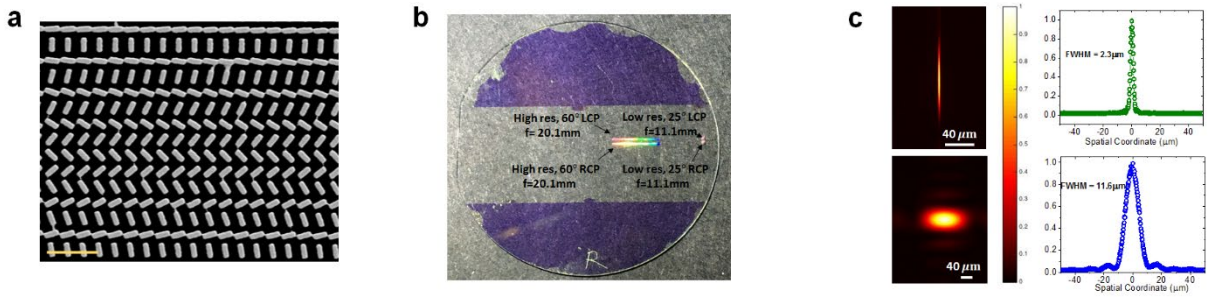

Fig. 4. Off axis metasurface lens (a) Scanning electron microscope (SEM) micrograph of off-axis metasurface lens. Scale bar: 800 nm. (b) Camera image of fabricated meta-lenses on a glass substrate, under white light illumination. A total of four lenses are made; high (0.22) and low (0.2) NA for each helicity of circular polarized light. Other parameters such as focal length and focusing angle are labeled. (c) Image of focal spots (left) captured by CMOS camera and their corresponding horizontal cuts (right). The focal spot spots (left images) are from the high NA (top) and low NA (bottom) lenses, respectively.

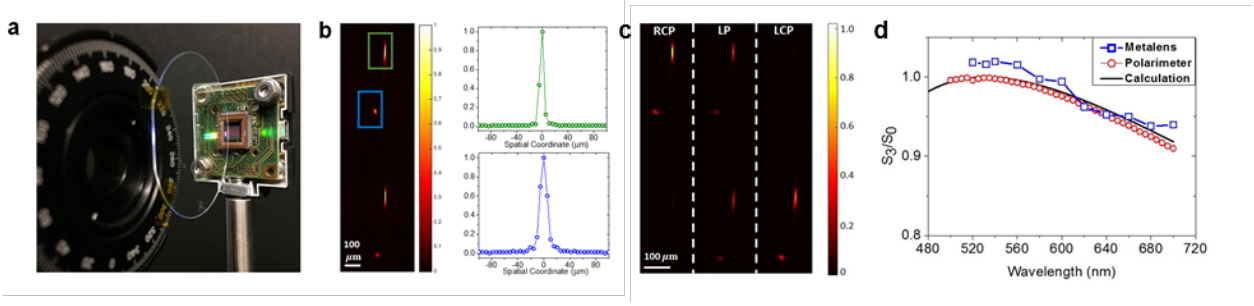

Fig. 5. Spectrometer set up (a) Camera image of the metasurface in a spectrometer setup. (b) Image of focal spots (left) and their corresponding horizontal cuts (right) at 532 nm illumination, following the configuration in (a). Cuts shown are for two spots belonging to lenses of different NA, with the same helicity. Focal spots from the opposite helicity are seen below. (c) Stitched image of focal spots at 532nm for different incident polarizations, by rotating a zero-order single wavelength (532 nm) quarter waveplate after a linear polarizer. The intensities of the RCP and LCP spots are observed to be slightly different due to fabrication imperfections as they are focused by different meta-lenses. Scale bar: 100 μm. (d) Further quantification of the chiral sensitivity of the device, showing the normalized *S*3/*S*0 Stokes parameter as a function of wavelength measured by the meta-spectrometer (blue), a commercial polarimeter (red), and theoretical calculation (black) from the known waveplate retardance. It exhibits a decrease in *S*3/*S*0 since the single wavelength waveplate is not designed to be achromatic, i.e. its retardance changes as a function of wavelength.

Figure 5 shows the fabricated meta-lenses mounted in a spectrometer configuration and their performance. Figure 5(c) and (d) demonstrate explicitly the polarization dependent focusing properties of this hyper-spectrometer. The polarization of the incident light is controlled using a linear polarizer and zero-order single wavelength (532nm) quarter waveplate. In Fig. 5 (c), as the incident light polarization is changed by rotation of the quarter waveplate, the respective focal spots exhibit strong intensity variations, i.e. light of different helicities are distinguished by the (chiral) meta-lenses and selectively focused onto different spatial regions on the camera. Next, we obtained the various S_3 Stokes parameters (which provides direct information on the degree of circular polarization) normalized to incident light intensity S_0 at different wavelengths using the meta-lenses and compared them to the results of a commercial polarimeter and analytical calculations (Fig. 5(d)). We observe that the measured values are in good agreement with both the values measured by the polarimeter and analytical predictions based on known retardance data.

D. Giant intrinsic chiro-optical activity in planar dielectric nanostructures

A key requirement for observing chiro-optical effects is the superposition of the radiated fields from both electric and magnetic responses in a structure under illumination (Fig. 6 (a-c). This can be achieved with any three dimensional (3D) chiral metamaterial, as the vertical part of the structure supports electric current loops which generate in-plane magnetic moments. The resultant radiation possesses field components which have non-zero overlap, thereby resulting in polarization rotation and optical activity. This phenomenon is known as intrinsic chirality. However, this suggests that intrinsically chiral objects are constrained to possess a 3D geometry, and they thus suffer from significant fabrication complexity,

particularly at optical frequencies. Indeed, most of such works have occurred in THz and GHz regimes and are non-scalable. Alternatively, it has been shown that chiro-optical effects can also be realized with planar chiral metasurfaces, but only by restricting the external experimental configuration to oblique angles of incidence or observation. This is known as extrinsic chirality and can be understood from symmetry considerations as well as the superposition argument mentioned previously. However, the fact that their chiro-optical responses vanish at normal incidence is a crucial limitation, particularly for applications such as telecommunications.

Recently we have overcome the inherent limitations associated with both 3D and planar chiral metamaterials by using planar dielectric gammadion nanostructures whose electromagnetic response is dominated by exceptionally strong electric and magnetic higher order multipole responses in the visible spectrum. In contrast to conventional wisdom, the chiro-optical response of these structures is intrinsic, i.e. it manifests at normal incidence and does not depend on the direction of incident light. We show that theoretically one can obtain close to unity circular dichroism with more than 95% of light of a given helicity being transmitted; experimentally we measure close to 80% circular dichroism and polarization rotation exceeding 100,000°/mm (Fig. 6 (d, e). These values not only exceed the state-of-the-art for chiral metasurfaces by up to an order of magnitude, they are also comparable to 3D chiral metamaterials which have far more complicated geometries and operate at much lower frequencies.

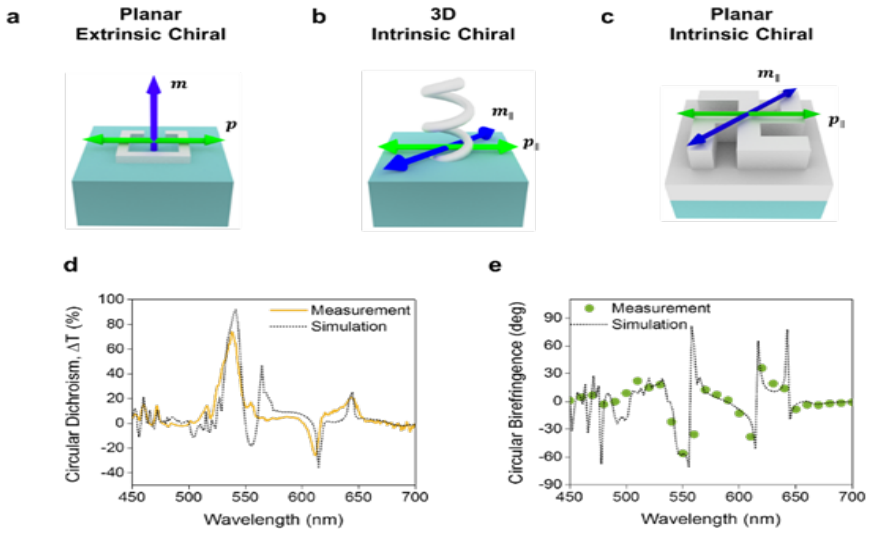

Fig. 6. **Chiroptical activity**. a-c Illustrations of electric and magnetic moments generated in (a) a planar extrinsic (also known as pseudo chiral) chiral metasurface, (b) an intrinsically chiral metamaterial, and (c) an optically thick planar structure which exhibits intrinsic chirality, despite its planar geometry. This is the subject of this work. d-e Measured (d) circular dichroism values of the differential transmittance, and (e) polarization rotation of linearly polarized light due to circular birefringence.

The design of the gammadion (Fig. 1(c)) is based on the concept of magnetic resonances in high-index, optically thick (~ λ) dielectric nanostructures. This allows one to generate strong in-plane magnetic moments while maintaining a 2D geometry. The superposition of radiated fields from these magnetic and electric responses of the chiral structures (Fig. 7) generates the chiro-optical effect. An additional waveguiding layer using the same material (titanium dioxide) is introduced beneath the structures to improve the transmission efficiency via guided mode resonances.

Experimentally we utilized a supercontinuum laser source at normal incidence with a commercial spectrometer and polarimeter as detectors. Figure 6(d) illustrates the measured and simulated circular dichroism spectrum corresponding to the 0th order transmittance (normal to the surface of the sample). We obtain 80% circular dichroism at 540 nm, with about 87% of right circularly polarized light transmitted through the sample. The incident left circularly polarized light is almost completely into the 1st diffraction order by design.

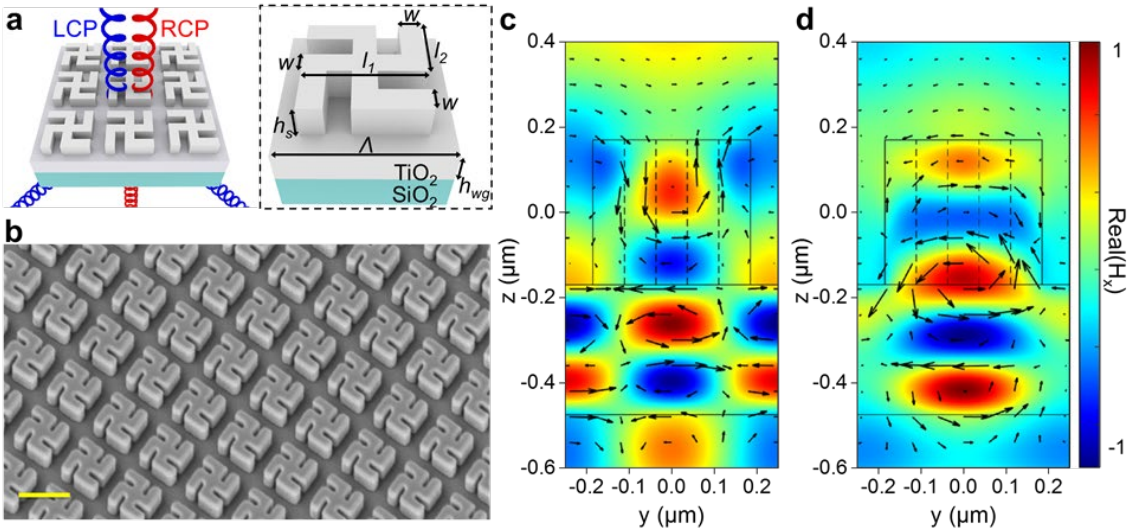

Fig. 7. **Design and simulation of gammadion nanostructures**. a, (Left) Schematic of the optical response of the planar intrinsic chiral device comprising of TiO2 gammadions overlaid on a TiO2 thin film on a glass substrate. It transmits normally incident RCP light (red helix) in the 0th order while diffracting LCP light (blue helix) into the 1st order. (Right) Design parameters are w = 74 nm, l1 = 370 nm, l2 = 220 nm, hs = 340 nm, hwg = 300 nm. The unit cell size Λ is 500 nm. b, Tilted-view scanning electron micrograph of the fabricated structures. Scale bar: 500 nm. c,d, y-z cut-plane showing the simulated in-plane magnetic field Hx (color plot) and the associated current distribution Jz+Jy (black arrows) in the gammadion structures under (c) LCP and (d) RCP incidence. The rectangular outline from z = 0.17 μm to z = -0.17 μm represents the gammadion structure, with subsequent layers below being the TiO2 waveguide and substrate respectively. The difference in the number of antinodes of Hx within the structure illustrates its chiral behavior due to different multipoles (quadrupoles and octupoles) when illuminated with different circular polarization states.

These values agree well with simulations. A peak polarization rotation of almost 60° for a combined structure and waveguide thickness of 600 nm is achieved. As a reference, the polarization rotation of most natural materials is on the order of degrees per mm.

E. Metasurface polarization optics: independent phase control of arbitrary orthogonal states of polarization

A metasurface composed of optical elements with shape birefringence, such as the rectangular nanofins of Fig. 8, act as a different optical element depending on the polarization of incident light. From a technological standpoint, this exciting capability allows for a new class of polarization-switchable optical components. In this work, we showed that the geometric and propagation phases used in tandem allow for the imposition of arbitrary phase profiles on any two orthogonal polarization states (linear, circular, or elliptical), significantly expanding the scope of metasurface polarization optics and allowing for new polarization switchable metasurfaces such as novel chiral holograms.

We begin by considering the propagation phase alone. At each point on a metasurface, the characteristic phase shifts ϕ_x and ϕ_y imposed by an element can be individually tailored by adjusting its shape while its angular orientation θ is held fixed. In this way, arbitrary and independent spatial phase profiles can be imposed on any set of orthogonal, linear polarizations using the so-called propagation (or dynamical) phase [Fig. 8(a)]. The propagation phase is one of two means of imposing polarization-dependent phase. The other, the geometric phase, stems from polarization change (Fig. 8b).

In contrast to previous designs using propagation or geometric phase alone, this allows for metasurfaces imparting fully independent phase profiles separately on each of any two orthogonal polarizations (including circular and elliptical). It can be understood as a unification of the propagation and geometric phases in a single element. Desired phases can be imparted on any set of orthogonal polarization states by modifying an element's shape birefringence and angular orientation simultaneously [Fig. 8(c)].

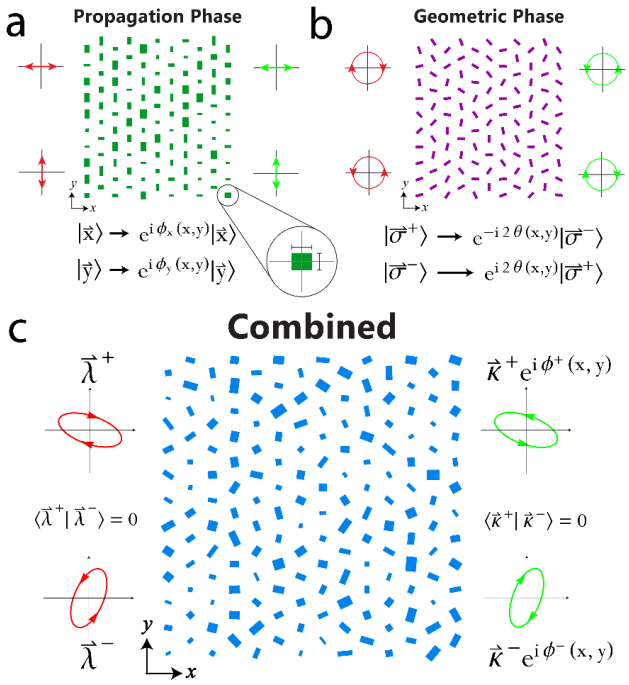

Fig. 8. **Conceptual schematic of combining propagation and geometric phase**. (a) At each point (x,y) on a metasurface, the dimensions of a wave plate-like shape-birefringent element (inset) can be varied to impose unique phases ϕ_x and ϕ_y on light linearly polarized along each axis. In this approach, which employs the propagation phase alone, element dimensions are varied while the orientation angle θ is held fixed. When each of two orthogonal, linear input polarizations (red, on left) (b) Using the geometric phase alone, phase profiles of equal and opposite magnitude can be imparted on the two circular polarizations. If elements with half-wave (π) retardance are rotated at angles θ(x,y)at each point, one input circular polarization (red, on left) will pick up a phase of 2θ(x,y) and the other −2θ(x,y) with each changing handedness upon reflection or transmission (green, on right). Here, element dimensions are fixed and the orientation θ is varied. (c) By varying both element dimensions and θ over the extent of the metasurface—that is by combining the geometric and propagation phases—we show that arbitrary and independent phase profiles ϕ(x,y) can be imparted on any set of orthogonal input states $\lambda^{\pm}$ (red, on left). Each must flip handedness upon reflection or transmission (green, right).

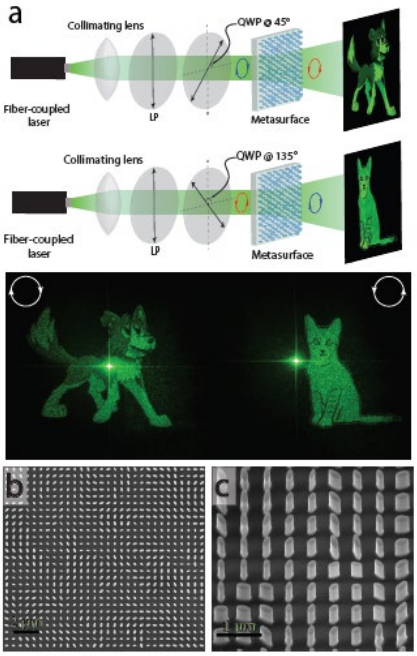

Fig. 9. Chiral Holograms. (a) A single metasurface encodes two independent hologram phase profiles for each circular polarization at λ=532 nm. When illuminated with RCP (LCP), the metasurface projects an image of a cartoon dog (cat) to the far field. Design images are shown in the schematic (top) and measured projections on a screen are shown below. The dog (cat) occupies 17° (15°) of arc. The bright dot in the center of each represents zero-order light not coupling into the metasurface due to fabrication imperfections and beam overfilling. (b) The metasurface encoding these holograms was 350 × 300 μm in size and contained 420 000 TiO2 pillars of elliptical cross section. Shown is an SEM of the device. (c) Oblique view.

To demonstrate this arbitrary phase control for polarizations other than linear polarizations, we designed, fabricated and tested a metasurface encoding separate holograms for RCP and LCP light (Fig. 9). The near-field phase profiles yielding far-field intensity images of a cartoon cat and dog were computed using iterative phase retrieval and a metasurface consisting of non-interacting, elliptical TiO2 pillars was designed to impose these phase profiles independently on each circular polarization in transmission.

F. Spin-to-orbital angular momentum conversion in dielectric metasurfaces

Vortex light beams are used in many applications in optics, ranging from optical trapping to quantum computing and telecommunications. A helical mode is an optical field whose azimuthal phase evolution along the propagation axis (z) has the form $exp[il\varphi]$, φ being the azimuthal angle and l (an integer). Vortex beams carry an orbital angular momentum per photon of $\ell\hbar$. Moreover, as any other light beam, circularly polarized helical modes also carry a spin angular momentum per photon of $\pm\hbar$, depending on the polarization handedness. These features have found numerous applications in studying light matter interactions like optical trapping where the angular momentum transfer represents a powerful manipulation tool to spin the trapped objects as well as to control their orientation.

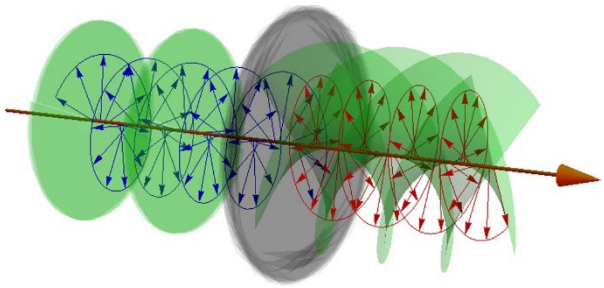

Fig. 10 Schematic of the working principle of a spin-orbital angular momentum converter. A left circularly polarized beam with plane wavefront is turned into a right circularly polarized helical mode.

We have realized devices made of dielectric sub-wavelength resonators on glass substrates designed to convert an incident Gaussian beam into a vortex beam with high-efficiency in the visible light spectrum (Fig. 10). Our devices exploit the geometrical phase principle to couple the light spin momentum of the incident beam to the orbital angular momentum of the vortex beam. In such devices, the orbital angular momentum of the vortex beam is related to the spin momentum of the illuminating light: switching the handedness of the illuminating beam polarization (spin momentum) results in flipping the handedness of the vortex beam topological charge. The way to impose a helical phase on an incident circularly polarized beam using a Berry phase metasurface has been illustrated in the summary of accomplishments section.

Locking the vortex beam's orbital angular momentum to the source beam's spin momentum has unique applications in quantum computing and communications.

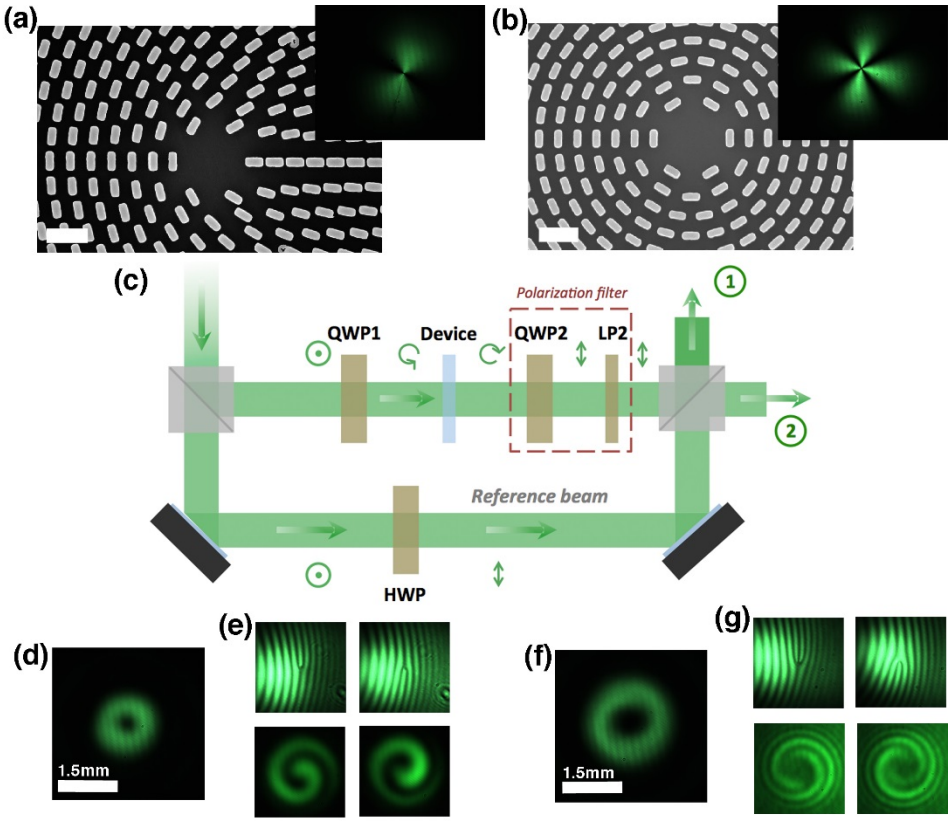

Fig. 11. Spin-to-orbital angular momentum converters (a) and (b), Scanning electron microscope image of TiO_2-based spin-orbital angular momentum (OAM) converters creating circularly polarized helical beams of OAM 1 and 2 respectively (scale bar = 650 nm). The insets show the devices observed in cross-polarization at the design wavelength of 532nm. (c), Sketch (top view) of the interferometric setup used to characterize the devices. The interference of the helical mode and the reference gaussian beam was monitored at port 1 by means of a CCD. The polarization state of the beam after each optical element is sketched. The laser polarization is linear and perpendicular to the optical table. Light becomes circularly polarized after the first quarter waveplate (QWP1). The helical mode generated by the device is circularly polarized with opposite handedness. The helical mode after the polarization filter (QWP2 followed by LP2) is linearly polarized parallel to the optical table. The reference beam in the lower arm of the interferometer becomes also linearly polarized parallel to the optical table after passing through a half waveplate (HWP) that rotates the polarization direction by 90°. (d), Transverse intensity distribution of the vortex beam generated by the device of Fig. 11(a). This beam has an OAM equal to 1. (e), Interference patterns obtained with tilted reference beam (pitchforks) or collinear reference beam (spirals) in the setup of (c). The flipped features result from opposite handedness of the beam that illuminates the device. (f), (g), Same as (d) and (e) for the device in (b).

G. Arbitrary spin-to-orbital angular momentum conversion of light

Geometric phase elements of the type described in the previous section provide a direct connection between optical SAM and OAM. These devices have broadened the applications of optical OAM, including its direct generation from laser cavities and new quantum devices. Due to the symmetry of the design (only the constituent elements' rotation angles vary) all SOC demonstrated thus far have two inherent limitations. First, the output OAM states are not independent; they are constrained to be conjugate values ($\pm 2q\hbar$). Second, the mapping from SAM is limited to circular polarizations, only two of an infinite set of possible polarizations.

Here, we have demonstrated the design of an optical element that overcomes these limitations and provides conversion from any orthogonal polarizations to completely independent OAM states. We refer to this as arbitrary SOC since there are no restrictions on the two orthogonal input SAM states and output OAM states. This contrasts with previous SOC devices that have used arbitrary to mean a device with any value of conjugate OAM, while still having the limitations detailed above. We implement this design using metasurfaces because of their ability to control polarization and phase. We examine the output fields of the device and show that this technique provides for arbitrary superpositions of two TAM states. Because of its ability to map an arbitrary input SAM to two arbitrary output TAM states (where TAM is typically represented by the variable γ), we refer to this device as a J-plate.

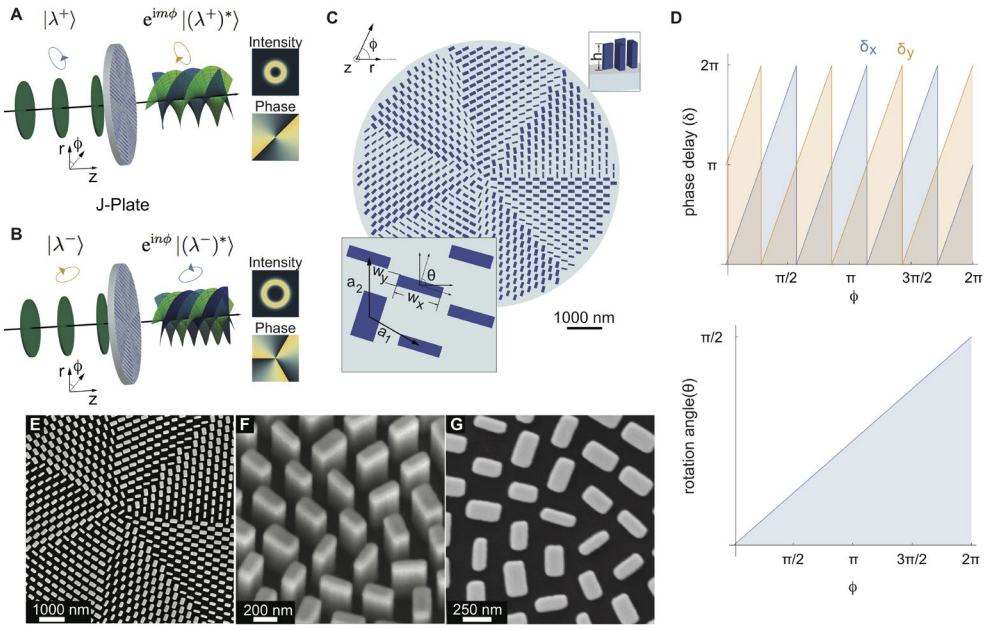

Fig. 12 Arbitrary spin-to-orbital angular momentum conversion. (A) Schematic of the concept for arbitrary SOC. Light with an arbitrary spin state (elliptical polarization), λ^+, propagating along the z-axis is incident on the J-plate. The J-plate imprints a helical phase profile on the output beam resulting in orbital angular momentum (OAM) mħ, where m is any integer, and flips the handedness of the incident polarization. (B) For light incident on the same device with an orthogonal polarization state λ^-, the device imprints OAM of nħ, where in general n is independent of m and again flips the handedness of the polarization. (C) Schematic of typical J-plate design used to carry out the function in (A) and (B). The units have a given height, h, (top inset) and by changing their width along the x and y directions, w_x and w_y (bottom inset) the structures implement phase shifts given by δ_x and δ_y, respectively. Each unit is also allowed to have an independent orientation angle, θ. (D) Required phase shifts, δ_x and δ_y (top) and rotation angle (bottom) as a function of the azimuthal coordinate φ. The case plotted here is for designed input spin states that are left and right circularly polarized and for OAM states m = +3 and n = +4. (E-G) Scanning electron micrographs of fabricated device for the case of mapping from circularly polarized states to helical beams with OAM values of m = +3 and n = +4. The SEMs show a top view (E) angled view (F) and zoomed view of the device center (G)

Figure 12 A and B show a schematic of the mapping carried out by the J-plate. We consider an incident paraxial beam propagating along the +z-direction. If the incident beam is in some arbitrary polarization state $|\lambda\hat{}+\rangle$, which in general is a superposition of spin eigenstates, we require the device to perform the transformation $|\lambda^+\rangle \rightarrow \exp(im\phi)\ |\lambda^+\rangle^*$, that is, the output has opposite handedness, and the beam has acquired an azimuthally-dependent phase factor exp(imϕ), where m is any integer (Fig 1A). The output beam has m helically-intertwined phase fronts (mħ OAM) and an annular intensity profile (Fig. 1A, right inset). If a beam in the orthogonal SAM state, $|\lambda^-\rangle$, is incident on the same device we require that it yields an independent OAM state. This is shown in Fig. 12B, where the mapping is $|\lambda^-\rangle \rightarrow \exp(in\phi)|(\lambda^-)^*\rangle$. The output has acquired an azimuthal phase factor of exp(inϕ) (OAM nħ), independent of m.

We have derived the Jones matrix J that performs this mapping. It is easily found that J (φ) $|\lambda+\rangle$ = exp(imφ) $|(\lambda^+)^*\rangle$ and J (φ) $|\lambda^-\rangle$ = exp(inφ) $|(\lambda^-)^*\rangle$, as desired. No traditional optical element can provide the required controllable and continuous spatial variation of phase shifts, birefringence, and orientation angle of the fast axis. Metasurfaces, however, which are composed of subwavelength-spaced, birefringent phase-shifters, allow for such control. This concept is illustrated in Fig. 12 C. Nanostructures of TiO_2 are arranged periodically in two dimensions with a fixed height h (top inset), while the phase shifts δ_x and δ_y on light linearly polarized along the elements' symmetry axes are controlled by varying the dimensions w_x and w_y. The orientation angle of each element θ can also be independently varied (bottom inset). An important distinction compared to SOC based on the geometric phase alone is that both the phase shifts and orientation angles vary as a function of φ, i.e., they are both spatially inhomogeneous, thus decoupling the output OAM states and input SAM.

For circular polarization, $\chi = \pi/4$ and $\delta = \pi/2$ and for any values of m and n, we can find analytical solutions for the required phase shifts and orientation angles as a function of φ, $\theta = 1/4\ (m - n)\ \varphi$; $\delta_x = 1/2(m + n)\varphi$, $\delta_y = 1/2(m + n)\varphi - \pi$. In Fig. 12D, we plot these equations as a function of φ for m = +3 and n = +4. We plot the variation of the phase shifts δ_x and δ_y, modulo 2π (Fig. 12D, top). We clearly see (m + n)2π phase rollovers, also observed in the device design itself (Fig. 1C). For the more general case of elliptical polarizations the solutions do not yield succinct expressions and must

be calculated for specific values of m, n, χ, and δ. To provide the most direct comparison to geometric-phase SOCs, we first demonstrate a device that converts from circularly-polarized input states to two output independent OAM beams. We choose the specific mapping to be |R) → |L) |+4) and |L) → |R) |+3), as in Fig. 12. We write the azimuthal phase factor exp(imφ) as |m) for brevity and to highlight that the J-plate output is a TAM state, a direct product between SAM and OAM states. The set of outputs from this J-plate can be represented on a sphere whose poles are the two output TAM states and all other points are superpositions of these two states. This sphere that combines both SAM and OAM is called the higher order Poincare´ sphere (HOPS) in contrast to the traditional Poincare´ sphere. Figure 13A shows the HOPS for the case above. The poles correspond to |R) |+3) and |L) |+4). All other outputs correspond to a point on the HOPS represented by the angular coordinates Φ and Θ (Fig. 4A). Figure 13 B-E show measured and calculated results verifying the operation of the J-plate. The labels (i-vi) correspond to the states indicated by the blue circles on the HOPS of Fig. 13 A. Figure 13 B(i) and (vi) and Fig. 4C(i) and (vi) show the measured and calculated intensities for incident left and right circularly polarized light, respectively. These intensity profiles are single ringed annuli with zero intensity as r → 0. The measured interference pattern corresponding to the intensities in Fig. 13 B(i) and (vi) are shown in Fig. 13D(i) and (vi). We observe 3 and 4 arms, in the spiral interference patterns which converge on the beam axis. Fig 13E(i) and (vi) show the calculated phase distribution of the two states, whose phase have 3 and 4 multiples of 2π around the azimuth. This is consistent with the two being pure OAM states and consistent with the two designed output states for this J-plate, |+3) and |+4). Notably these values are not conjugate.

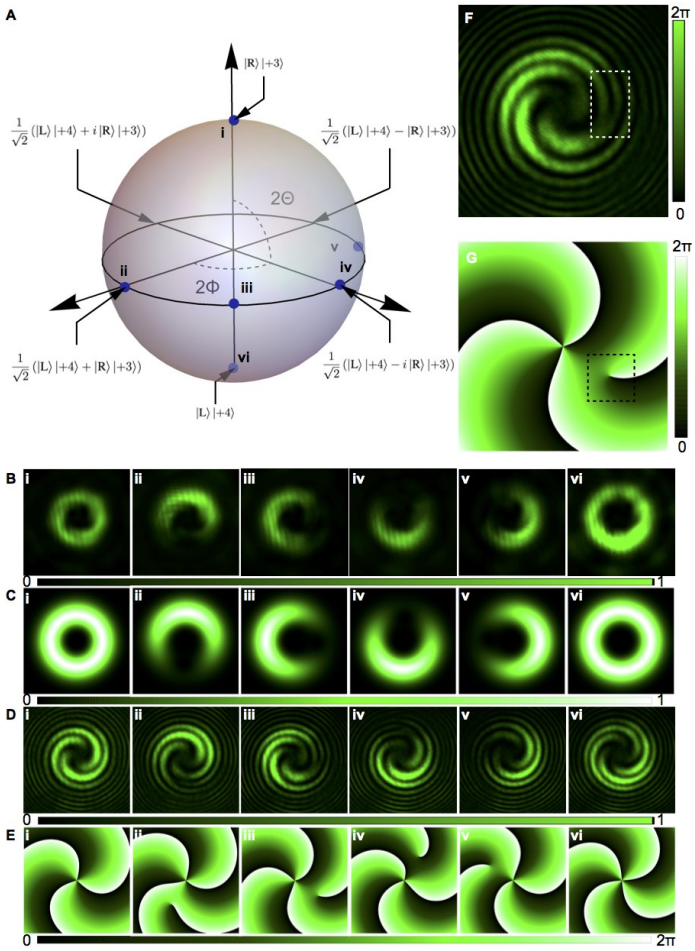

Fig. 13 Experimental demonstration of mapping from circular polarizations to two beams with arbitrary values of OAM. (A) HOPS representing all possible spin and orbital angular momentum states produced by a device that carries out the mapping |R> → |L> |4> and |L> → |R> |+3>. (B to E) Measured and calculated output states of the device. The output states are produced by using incident polarizations including left- and right-circular polarizations and four different linear polarizations. The states in (B) to (E), i to vi, are marked as blue circles on the HOPS in (A). (B) Measured and (C) calculated intensity of the output states. Scale bar below shows normalized intensity. (D) Measured interference and (E) calculated phase of output states. Scale bars below show (D) relative intensity and (E) the phase. (F and G) Expanded view of measured interference and calculated phase of intensity of output state in (D), iii, and (E), III. The dashed boxes highlight an additional vortex that results from the equal superposition of |+3>and |+4> states. This vortex results in (F) an off-axis fork in the interference pattern corresponding to (G) an additional off-axis 0 to 2p phase jump. The scale bar shows the value of phase.

4. Publications

1. M. Khorasaninejad, A. Ambrosio, P. Kanhaiya, F. Capasso "Broadband and chiral binary dielectric meta-holograms" *Science Advances 2*, 5 (2016)
2. M. Khorasaninejad, W.T. Chen, A.Y. Zhu, J. Oh, R.C. Devlin, D. Rousso, and F. Capasso "Multispectral Chiral Imaging with a Metalens" *Nano Letters* **16**, 4595 (2016)
3. Alexander Y. Zhu, Wei-Ting Chen, Mohammadreza Khorasaninejad, Jaewon Oh, Aun Zaidi, Ishan Mishra, Robert C. Devlin, and Federico Capasso, "Ultra-compact visible chiral spectrometer with meta-lenses" *APL Photonics* **2**, 036103 (2017)
4. J. P. Balthasar Mueller, Noah A. Rubin, Robert C. Devlin, Benedikt Groever, and Federico Capasso, "Metasurface Polarization Optics: Independent Phase Control of Arbitrary Orthogonal States of Polarization" *Physical Review Letters* **118**, 113901 (2017)
5. Robert C. Devlin, Antonio Ambrosio, Daniel Wintz, Stefano Luigi Oscurato, Alexander Yutong Zhu, Mohammadreza Khorasaninejad, Jaewon Oh, Pasqualino Maddalena, and Federico Capasso, "Spin-to-orbital angular momentum conversion in dielectric metasurfaces" *Optics Express* **25**, 377 (2017)
6. Mohammadreza Khorasaninejad, Wei Ting Chen, Alexander Y. Zhu, Jaewon Oh, Robert C. Devlin, Charles Roques-Carmes, Ishan Mishra, and Federico Capasso, "Visible Wavelength Planar Metalenses based on Titanium Dioxide" *IEEE Journal of Selected Topics in Quantum Electronics* **23**, 4700216 (2017) *Invited*
7. Patrice Genevet, Federico Capasso, Francesco Aieta, Mohammadreza Khorasaninejad and Robert Devlin "Recent advances in planar optics: from plasmonic to dielectric metasurfaces" *"Optica* **4**, 139 (2017), *Invited*
8. W-T Chen, A. Y. Zhu, M. Khorasaninejad, Z. Shi, V. Sanjeev, and F. Capasso, "Immersion Meta-Lenses at Visible Wavelengths for Nanoscale Imaging" *Nano Letters* **17**, 3188 (2017)
9. M. Khorasaninejad and F.Capasso, "Metalenses: Versatile multifunctional photonic components" *Science* **358**, 8100 (2017) *Invited Review*
10. W-T Chen, A. Y. Zhu, M. Khorasaninejad, Z. Shi, V. Sanjeev, and F. Capasso, "Immersion Meta-Lenses at Visible Wavelengths for Nanoscale Imaging" *Nano Letters* **17**, 3188 (2017)
11. A. Y Zhu, W-T Chen, Aun Zaidi, Y-W Huang, M. Khorasaninejad, V. Sanjeev, C-W Qiu, F. Capasso, "Giant intrinsic chiro-optical activity in planar dielectric nanostructures" *Light: Science & Applications, 7, 17158 (2018)*
12. R. C. Devlin, A. Ambrosio, N. A. Rubin, J.P. Balthasar Mueller, and F. Capasso "Arbitrary spin-to-orbital angular momentum conversion of light" *Science* **358**, 896 (2018)